Volume 6 | Number 26 | 14 July 2018 | Pages 12165–12796

Journal of Materials Chemistry A

Materials for energy and sustainability

rsc.li/materials-a

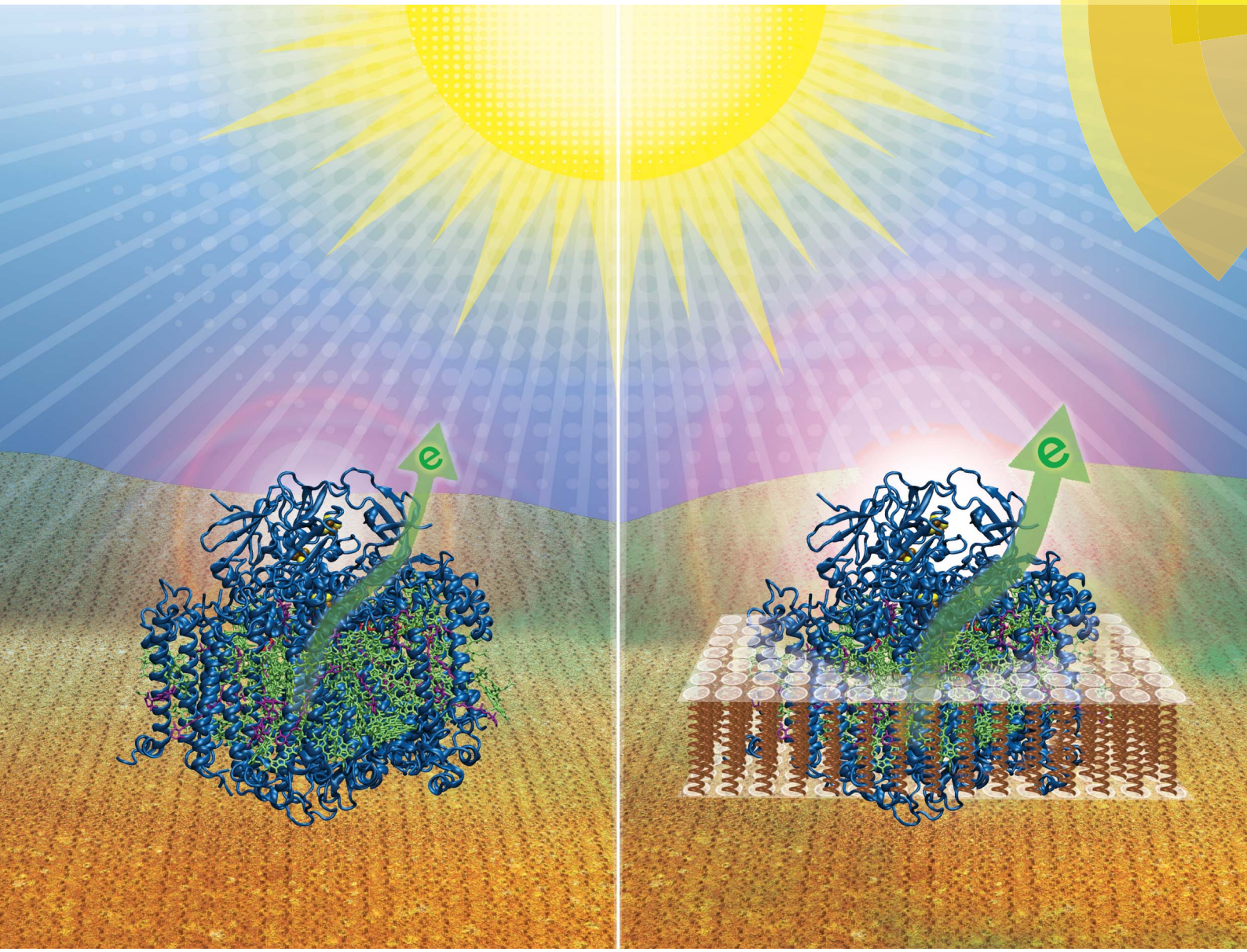

ISSN 2050-7488

ROYAL SOCIETY OF CHEMISTRY

PAPER

Dibyendu Mukherjee, Bamin Khomami *et al.*

Microenvironment alterations enhance photocurrents from photosystem I confined in supported lipid bilayers

Journal of Materials Chemistry A

PAPER

Cite this: J. Mater. Chem. A, 2018, 6, 12281

Microenvironment alterations enhance photocurrents from photosystem I confined in supported lipid bilayers†

Hanieh Niroomand, [ac] Ravi Pamu, [bd] Dibyendu Mukherjee *[abcd] and Bamin Khomami *[acd]

Received 27th January 2018
Accepted 10th April 2018

DOI: 10.1039/c8ta00898a

rsc.li/materials-a

Transmembrane photosynthetic proteins, photosystem I (PSI), are nano-scale biological photodiodes that enable light-activated unidirectional electron flow. The robust photochemical properties of PSI make it a promising candidate for harnessing solar energy. However, the role of natural membrane confinements of PSI in orchestrating this photoactivated charge separation with near unity quantum efficiency, which is central to the rational design of PSI-based energy conversion systems, is still ill-understood. Motivated by this lack of fundamental understanding, herein we investigate the photoactivity of biomimetic constructs of cyanobacterial PSI encapsulated within solid-supported lipid bilayers (SLB) assembled on electrodes. PSI confined in SLBs is assembled from PSI-proteoliposomes that are synthesized from our recently developed facile routes for engineering negatively charged phospholipid (DPhPG) bilayer membranes. Specifically, detailed chronoamperometry measurements have been used to investigate photocurrent variations arising from the SLBs supported on self-assembled monolayer (SAM) substrates. These measurements, in conjunction with cryo-transmission electron microscopy, atomic force microscopy imaging and force spectroscopy, allow for direct visualization and detection of the SLBs of PSI-proteoliposomes on the substrates. Our results indicate the critical role of microenvironment alterations, heretofore not considered, in achieving ~4–5 fold enhancements in photocurrents generated from PSI complexes under SLB confinements as compared to those from a dense monolayer of equivalent concentrations of PSI on SAM substrates.

Introduction

Natural oxygenic photosynthetic processes have been an inspiration for biomimetic and highly efficient solar to chemical energy conversion systems. To this end, several attempts have been made to reconstruct bio-hybrid photoelectrochemical conversion devices *via* optimal interfacing of inorganic electrodes with photosystem I (PSI), the transmembrane trimeric protein complex responsible for the photoactivated charge separation with near unity quantum efficiency during natural photosynthesis.[1] In recent years, a flurry of research has been focused on strategies for immobilizing PSI onto conductive materials (gold, titanium oxide, silicon, graphene, or gallium(III) arsenide (GaAs), carbon nanotubes (CNTs) or other nanoparticles, and redox polymers).[2–10] Furthermore, efforts have also been directed toward the genetic mutation of PSI to enable direct wiring of PSI to electrodes in order to fabricate efficient PSI-based bio hybrid photo-sensors.[11–15] In spite of the large volume of work on various chemical and inorganic routes to attach PSI to electrode substrates, these investigations have heavily relied on the use of some form of self-assembled monolayers (SAMs) of organothiol-based compounds to immobilize PSI films onto metal surfaces (mostly gold).[16–23] Thus, these efforts have been largely effective in depositing dense monolayers or multilayers of PSI with limited success in preferential orientation of PSI and high photocurrent generation from these systems. Although such efforts are commendable, a significant knowledge gap exists in the reliable verification of the orientation, long-term functionality and photoactivity of PSI to enable light-activated charge transfer with near unity quantum efficiency on these SAM-based assemblies. Such observations, in turn, have increasingly drawn attention towards the role of the natural thylakoid membrane scaffoldings in enhancing the efficiency, orientation and lifetimes of the photochemistry of the PSI trimeric complex deposited on various materials.

[a]Sustainable Energy Education and Research Center (SEERC), University of Tennessee, Knoxville, USA. E-mail: bkhomami@utk.edu; dmukherj@utk.edu; Fax: +1 865 974 7076; +1 865 974 5274; Tel: +1 865 974 2421; +1 865 974 5309

[b]Nano-Biomaterials Laboratory for Energy, Energetics & Environment (nbml-E[3]), University of Tennessee, Knoxville, USA

[c]Department of Chemical & Biomolecular Engineering, University of Tennessee, Knoxville, USA

[d]Department of Mechanical, Aerospace & Biomedical Engineering, University of Tennessee, Knoxville, USA

† Electronic supplementary information (ESI) available. See DOI: 10.1039/c8ta00898a

The efficient electron transfer between the oxidized and reduced redox partners of PSI occurs on opposite sides of the thylakoid membrane (namely the stromal and the lumenal sides), thereby mandating a specific protein orientation, while the specific protein conformation within the thylakoid membrane ensures the optimal stereochemistry for the inter-chromophore excitation energy transfer pathways.[24] Hence, the first step towards the successful fabrication of bio-hybrid devices capable of high photocurrent generation calls for the systematic assembly of oriented and functional PSI onto the desired bio–abio interfaces *via* suitable biomimetic protein scaffoldings. To this end, the current state of research in this area invokes the obvious question: does membrane confinement of PSI complexes serve a functional role apart from providing the structural scaffolds for the protein? Therefore, new techniques allowing for membrane reconstitution of PSI complexes to form stable proteoliposomes as the final product have become of great interest.

Typically, reconstituted proteoliposomes serve as experimental systems for the study of membrane enzymes[25] and small helical membrane proteins, providing a sample environment that accurately mimics the native membrane environment and properties such as hydrophobic thickness, water concentration and lipid order parameter gradients.[26,27] In the context of our study on reconstituted PSI, emerging studies include a recent study by Saboe *et al.* where PSI has been reconstituted in a two-dimensional crystal with a tethered bilayer lipid membrane support that indicated a 4-fold photocurrent enhancement through the incorporation of conjugated oligoelectrolyte (COE) units into this device.[28] In addition, the photo-bioelectrochemical impact of the direct incorporation of a series of COEs into thylakoid bioanodes resulting in up to 2.3-fold improvement in amperometric photocurrent density generation has been reported.[29] Moreover, enhanced photocurrent in PSI stabilized in and on a block copolymer support assembled on SAM/gold electrodes in the presence of COEs has also been reported.[30] Similarly, enhanced photocurrents in three-dimensional architectures of DNA molecules as scaffolds for PSI in conjunction with the redox protein cytochrome c (cyt c) assembled on mesoporous indium tin oxide (μITO) electrodes have been observed.[31] Specifically, this construct resulted in an internal quantum efficiency (IQE) of ~39%, one of the highest values reported for PSI assemblies on inorganic electrodes. Interestingly, this study attributed the high IQE values to efficient electron pathways inside the 3D transparent conducting architectures due to high protein loading.[32] But, what remains unclear in these intriguing results is the possibility of these significant photocurrent enhancements not only arising from the high packing density but also the orientation and confinement of PSI in these complexly tailored biomimetic organic/inorganic scaffolds. To this end, careful investigations of the exact role of specific membrane scaffolds and microenvironment alterations in tailoring the photoactive functionality and near unity quantum efficiency of PSI are much needed to address the protein conformational changes, if any, in its native membrane-bound form. In turn, such studies essentially leave us with the unanswered question regarding the biophysical role of membrane confinements in driving the optoelectronic dynamics and charge transfer properties of PSI.

Our main motivation in the present study stems from our recent studies providing direct evidence that PSI confinements in synthetic lipid scaffolds can be used to tune the photoexcitation characteristics of PSI.[33] This, in turn, has led to our recent efforts at attaining systematic incorporation of PSI complexes into synthetic membrane-bound structures that mimic the natural thylakoid membrane housing of PSI. Here, the central hypothesis is that PSI confinement in biomimetic membrane frameworks will allow tuning of inter-chromophore electronic coupling within the protein complex by many orders of magnitude through the optimization of chromophore separation and orientation. This is expected to promote photo-excited chromophore–chromophore energy transfer within the PSI and in turn, enhance photocurrent generation. The underlying mechanism behind such behaviors could be explained potentially, either *via* quantum coherence effects or stereochemical alterations in the chlorophyll network which is still under debate. To this end, as the first step towards investigating the optoelectronic behaviors of PSI confined under different bio–abio interfaces, the current study focuses on high density encapsulation of PSI in synthetic lipid bilayer membranes to constitute PSI-proteoliposomes followed by their immobilization onto bio hybrid electrodes and characterization of the photoelectrochemical response of the system. Specifically, a detailed investigation of photocurrent enhancements due to PSI confinement in DPhPG (1,2-diphytanoyl-*sn-glycero*-3-phospho-(1′-*rac*-glycerol)) liposomes assembled on specific alkanethiolate SAM (self-assembled monolayer)/Au surfaces is presented.

Experimental section

Materials

Dibasic (Na_2HPO_4) and monobasic (NaH_2PO_4) sodium phosphate with >99% assay purchased from Fisher Scientific were used to prepare the aqueous buffer solutions of 200 mM Na-phosphate with pH = 7.0. All aqueous buffer solutions of 200 mM Na-phosphate were prepared in ultrapure de-ionized (D.I.) water with a resistivity of 18.2 MΩ cm at 25 °C (Millipore, Billerica, MA). Triton X-100 (10% w/v aqueous solution) was obtained from Anatrace. DPhPG (1,2-diphytanoyl-*sn-glycero*-3-phospho-(1′-*rac*-glycerol)) was purchased as lyophilized powder from Avanti Polar Lipids, Inc. Carbon coated (400 mesh) copper grids were purchased from SPI supplies, USA. Gold coated silicon wafers, Au thickness ~100 nm were purchased from Platypus Technologies.

Methods

Growth of *T. elongatus* and preparation of photosystem I. The thermophilic cyanobacterium *Thermosynechococcus elongates* BP-1 was grown and extracted from thylakoids according to Kern *et al.*[34] The details of the extraction and purification of the trimeric PSI complex from the grown *T. elongatus* cells are provided elsewhere.[31] Based on spectrophotometer measurements of

chlorophyll concentration, the concentration of the extracted PSI trimers is estimated to be around 20.0×10^{-6} mol l^{-1}.

Liposome preparation. 4 mg ml^{-1} lipid suspensions were prepared in 200 mM Na-phosphate (pH = 7.0) buffer, followed by 3–4 freeze–thaw cycles to form multilamellar liposomes. These suspensions were then extruded through a 100 nm pore size filter using a NanoSizer Extrusion Kit (T&T Scientific) to form unilamellar vesicles at room temperature. The large unilamellar vesicle sizes of ~100 nm were confirmed *via* dynamic light scattering (DLS) measurements. Further details regarding the lipid vesicle preparations can be found in previous studies.[35]

Negative-staining electron microscopy (NS-EM). Negative staining was used to facilitate electron microscopy imaging by embedding and supporting a thin layer of the biological sample on a dried layer of heavy metal-containing salt, thereby increasing the contrast of the biological material with its surroundings without causing structural alteration. A sequential two-droplet method was used for negative staining. Aliquots (~5 μl) of the lipid/detergent in buffer suspensions were adhered to thin carbon-coated 400-mesh copper grids that were glow-discharged for 20 s to render them hydrophilic. The suspension was incubated for 1 min at room temperature. The excess sample solution was removed by blotting with a filter paper touched to the edge of the grid. After removing the excess fluid, the grid was stained with 1% (w/v) uranyl acetate (UAC) at pH = 3.0 for 60 s. Then the grid was dried at room temperature. Negatively stained specimens were examined with a Zeiss Auriga FIB-SEM microscope operated at 30 kV in STEM mode.

Reconstitution of PSI. Detergent-mediated protein reconstitution was performed by addition of a prototypical non-ionic detergent Triton X-100 (TX-100) to preformed liposomes (4 mg ml^{-1}).[36] The solution was equilibrated for 60 min, then mixed with the solubilized protein in 200 mM Na-phosphate buffer (pH 7.0), and afterwards, the mixture was incubated for 30 min at room temperature under gentle agitation. The final protein-to-lipid weight ratios used for all our studies (protein to lipid weight ratios or wPLR) were 1.2. For PSI reconstitution, TX-100 was slowly removed by a two-step procedure, *i.e.*, an addition of 15 mg bio-beads per milligram of TX-100 for 1 hour at room temperature and 12 hours at 4 °C, followed by an addition of 15 mg bio-beads per milligram of TX-100 at room temperature to ensure full detergent removal. Then, size-exclusion chromatography fractions were collected using a Sephacryl S-400 column attached to an AKTA purifier (GE). A total of 200 μl of sample was loaded at a flow rate of 0.5 ml min^{-1}. The sample elution was monitored at optimal wavelength for liposome and PSI absorbance at 540 and 680 nm, thereby enabling the detection of both PSI and lipids.

Cryo-transmission electron microscopy (cryo-TEM). The sample preparation for cryo-TEM was carried out on 200-mesh carbon-coated holey grids. Before the sample application, a glow discharge was performed in order to hydrophilize the grid for the optimal spreading of the aqueous sample. The suspension was then dropcast onto TEM grids following which the excess sample was absorbed using a filter paper, leaving a thin film of the sample in the holes of the grid. Then, the grid was mounted in a Gatan cryo-plunge 3 device and immediately frozen by plunging it in liquid ethane cooled by liquid nitrogen. After vitrification, the frozen-hydrated specimen was inserted into the Gatan cryo-transfer system and transferred into the TEM system. The imaging was carried out using a Zeiss Libra 200 MC TEM equipped with a model Gatan 915 cryo-specimen holder, at an acceleration voltage of 200 kV, and a temperature of about −170 °C under strict low dose conditions (<15 e $Å^{-2}$). Images were recorded with a Gatan UltraScan 1000XP. Quantitative analyses on more than $n > 30$ particles were used to measure the particle size at each stage of solubilization.

Preparation of alkanethiolate SAM/Au substrates. Commercial Au coated Si wafers (Au layer thickness ~10 nm, Platypus Technologies) were dipped in freshly prepared Aqua Regia (concentrated HCl and HNO_3 acids in a volumetric ratio of 3 : 1 respectively) prior to adsorbing thiols onto the surface. Freshly cleaved Au substrates (Au thickness ~60–70 nm) were then immersed in a 5 mM ethanolic solution of 4-mercaptobutyric acid (HS–C_3H_6–COOH, Sigma-Aldrich), 4-mercapto-1-butanol (HS–C_4H_8–OH, Sigma-Aldrich) and 6-mercapto-1-hexanol (HS–C_6H_{12}–OH, Sigma-Aldrich) for 7 days at room temperature in a chamber filled with inert dry N_2. Thiolated Au substrates were washed in isopropanol (electronic grade residue free; 99%), de-ionized water, and finally dried under a stream of dry N_2. Monolayer formation was confirmed by measuring the thiol thickness on Au substrates at multiple spots using a spectroscopic ellipsometer and was determined to be 0.53 ± 0.09 nm, 0.46 ± 0.16 nm and 0.62 ± 0.08 nm for C_4–COOH, C_4–OH and C_6–OH respectively.

PSI-proteoliposome deposition on the alkanethiolate SAM/Au substrates. 150 μl of protein-lipid suspensions were dropcast on the alkanethiolate SAM/Au substrates and incubated for 1 hour at 45 °C. Then, the samples were left at room temperature to cool for 1 hour, thereby allowing the surface assembly of PSIs incorporated within the supported lipid bilayers (PSI-SLB). Subsequently, PSI-SLBs were washed several times at room temperature with Na-phosphate buffer and de-ionized water.

Atomic force microscopy (AFM). AFM topographical characterization of PSI-proteoliposome treated Au substrates was carried out on commercial gold coated silicon wafers, Au thickness ~100 nm. Gold wafers were cleaned by immersion in isopropanol (99.99% v/v) and de-ionized water for 10 min, and drying in a N_2 stream. Surface immobilization of PSI-proteoliposomes was carried out by drop casting a few microliters of PSI-proteoliposome suspension after size exclusion chromatography on the Au wafers. The monolayer-covered gold wafer was allowed to dry for 1 hour at 158 °F and 1 hour at room temperature and then rinsed in de-ionized water and dried in a N_2 stream. Surface topography images were collected on an AFM instrument (NT-MDT) in the tapping mode using a silicon cantilever compatible with softer biological materials (NT-MDT; model: NSG03). The tip had a force constant of 0.35–6.1 N m^{-1} and a resonant frequency of 47–150 kHz.

Atomic force microscopy force spectroscopy (AFM-FD). Force–distance curves were obtained using flat gold wafers (Platypus Technologies) on an NT-MDT instrument in contact mode using sharp nitride SNL-10 cantilever tips (Bruker) with a nominal spring constant of 0.35 N m^{-1}. AFM images were

acquired at room temperature in de-ionized water. In force spectroscopy, as the AFM tip approaches a plastically deformable membrane on a hard surface, a discontinuity occurs in the approaching force–distance curve as the tip penetrates the membrane surface. The horizontal distance measured from the onset of the discontinuity to the hard surface repulsive curve is referred to as the breakthrough distance and is related to the membrane thickness. Multiple force–distance curves were obtained for each sample to ensure representative data.

Electrochemical and photoelectrochemical characterization. Electrochemical measurements were conducted using a bipotentiostat (make: Bio-Logic; model: SP-200) operated using the EC-Lab software. A glass electrochemical cell with a three-electrode configuration was used that carried a Pt wire counter electrode, a Ag/AgCl (sat. KCl) reference electrode (BAS Inc.; model: MF-2052 with a reference shift +0.197 V *vs.* NHE) and a Au substrate as the working electrode with the specific surface treatments (*i.e.*, SAM/Au, and PSI as well as PSI-SLB on SAM/Au electrodes). Except where specified, all electrochemical measurements were carried out in 200 mM Na-phosphate aqueous buffer (pH = 7.0) as the standard electrolyte to prevent any protein denaturation. Chronoamperometry (CA) data were collected at a bias of +0 V *vs.* reference and idled for 15 min before exposing the PSI-SLB/SAM/Au electrodes to light on/off conditions with 2–5 minutes pulses. This potential was chosen to facilitate the photoresponse solely from PSI. This bias is close to the open circuit voltage (OCV) for all tested PSI-SLB/SAM/Au electrodes, with minor background current shifts. We note here that the OCV shifts at varying solution content and concentrations, as well as upon surface modifications. A constant bias voltage was chosen over OCV to control the energy gap at the electrode surface, which greatly affects the electron transfer kinetics to and from PSI or methyl viologen (MV). 1 mM methyl viologen (MV) was added as the electron scavenger. All data were measured under dark, room temperature conditions except for the light experiments where the measurements were taken while the working electrodes were under illumination from an LED source (ThorLabs; model: M660L4) with a nominal intensity of 1000 W m^{-2} (λ = 660 nm).

Results and discussion

Illustrating the arrangements of the immobilized PSI-proteoliposome systems, Fig. 1 depicts the typical hierarchical assembly of PSI complexes in synthetic membrane-bound PSI structures on SAM-mediated electrode substrates. This figure also displays the anticipated electron transfer pathways for the oriented PSI systems.

The presence of trimeric PSI complexes, as extracted from cyanobacterial cultures (details in the Experimental section), was first confirmed using negative-staining electron microscopy (NS-EM) as shown in Fig. 2 that also shows the typical structure and dimensions of a PSI trimer as revealed by previous crystallographic studies. Subsequently, PSI-proteoliposome reconstitution was carried out by incorporating PSI solubilized with a prototypical non-ionic detergent namely, Triton X-100 (TX-100) into liposomes destabilized with TX-100 at detergent concentrations of C_{Trit} = 4.0, 8.0 and 12.0 mM. Lipid, detergent and protein concentrations for the successful reconstitution process have been described in detail in our recent work on surfactant induced DPhPG solubilization.[33] Following the PSI insertion, the excess detergent was adsorbed using polystyrene beads. All protein reconstitutions were performed at protein-to-lipid weight ratios of 1.2 (chosen based on our earlier study).[33] Then, size-exclusion chromatography (SEC) fractions were collected prior to any PSI-proteoliposome analysis. Specifically, PSI-proteoliposomes were separated from individual PSIs, small aggregates or excess detergents based on their physical size differences (data are shown in our earlier work).[33] Subsequently, cryo-transmission electron microscopy (cryo-TEM) imaging of a droplet of the suspension after SEC also corroborates the successful PSI-proteoliposome formation (as marked by arrows in Fig. 3a and b). Cryo-TEM micrographs of DPhPG liposomes show a delineated 3.3 ± 0.37 nm lipid bilayer wall (Fig. 3a) as compared to the cryo-TEM micrographs for PSI-proteoliposomes that clearly indicate the formation of regularly shaped unilamellar liposomes with a delineated 9 ± 0.91 nm lipid bilayer wall (Fig. 3b). This bilayer enlargement can be attributed to the incorporation of PSIs within the bilayer.

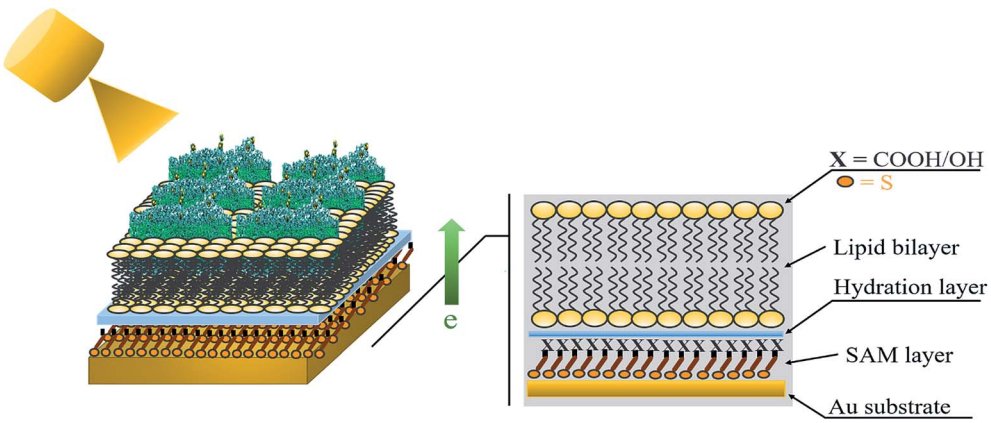

Fig. 1 Schematic representation of a typical PSI-SLB/SAM/Au electrode assembly along with the anticipated electron transfer pathway.

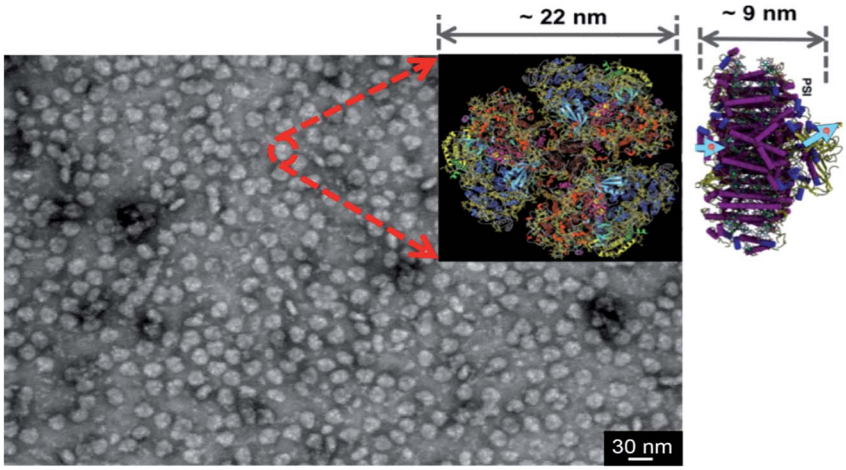

Fig. 2 Stained-TEM micrograph representing individual PSI trimeric complexes from cyanobacterial strains. (Top) Typical structure and dimensions of a PSI trimer from crystallographic studies.

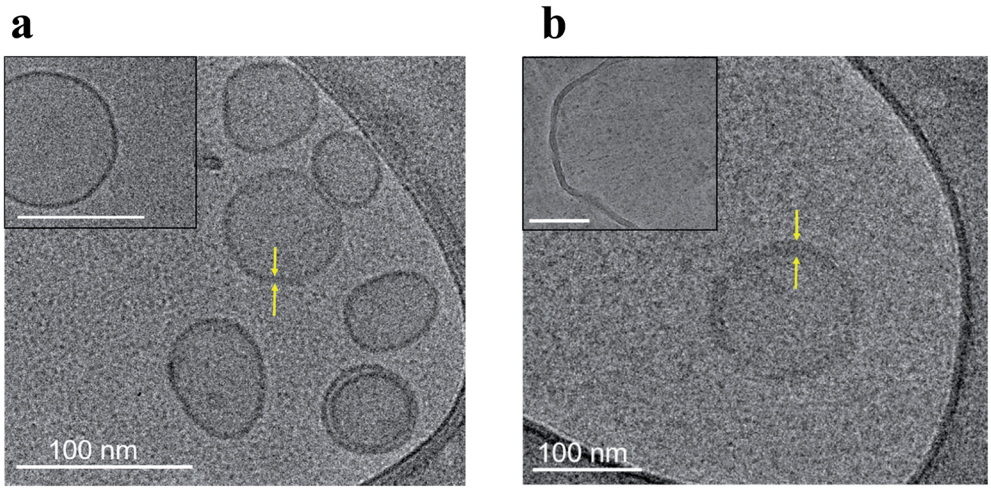

Fig. 3 Cryo-TEM micrographs of: (a) preformed DPhPG liposomes and (b) PSI-proteoliposomes. Scale bar, 100 nm.

To assemble the PSI-SLB (*i.e.*, PSI incorporated within supported lipid bilayers) electrode, PSI-proteoliposome suspensions collected from SEC fractions were dropcast onto OH- and COOH-terminated thiol SAM/Au substrates (see the Experimental section). Detailed technical specifications regarding the physical properties of 4-mercaptobutyric acid (C_4–COOH), 4-mercapto-1-butanol (C_4–OH) and 6-mercapto-1-hexanol (C_6–OH) are provided in Table 1.

Photoelectrochemical characterization of PSI-SLB electrodes

Chronoamperometry (CA) measurements were carried out on PSI-SLB/C_4COOH SAM/Au, PSI-SLB/C_4OH SAM/Au and PSI-SLB/C_6OH SAM/Au electrodes under light and dark conditions with the addition of methyl viologen (MV) as the electron scavenger under aerobic conditions. MV acts as an electron acceptor from the reducing (stromal) side of PSI.[23] Here, the aerobic conditions refer to the ambient equivalent levels of dissolved oxygen (O_2) in the buffer electrolyte solution. Furthermore, Fig. 4 shows the action spectra recorded for the PSI-SLB/SAM/Au electrode samples by measuring the photocurrent at 9 wavelengths (395, 420, 455, 470, 565, 660, 680, 730 and 810 nm) corresponding to the room temperature absorption spectra of the PSI suspension. The maximum photocurrent at 455 nm and 680 nm matches the PSI absorption spectra, thereby verifying the integrity of PSI in its native form during the reconstitution and immobilization on the gold substrates.

Table 1 Physical properties of SAMs, C_4–COOH, C_4–OH and C_6–OH

Chemical name	Linear formula	Molecular weight
4-Mercaptobutyric acid	$HS(CH_2)_3COOH$	120.17
4-Mercapto-1-butanol	$HS(CH_2)_4OH$	106.19
6-Mercapto-1-hexanol	$HS(CH_2)_6OH$	134.24

Fig. 5 shows that in the presence of MV and dissolved O_2, a stable net photocurrent of ~14.5 nA cm^{-2} (negative directions as compared to baseline current) is achieved in the case of the PSI-SLB/C_4COOH SAM/Au electrode, while a stable net photocurrent of ~18 nA cm^{-2} and ~20 nA cm^{-2} is obtained in the case of PSI-SLB/C_4OH SAM/Au and PSI-SLB/C_6OH SAM/Au

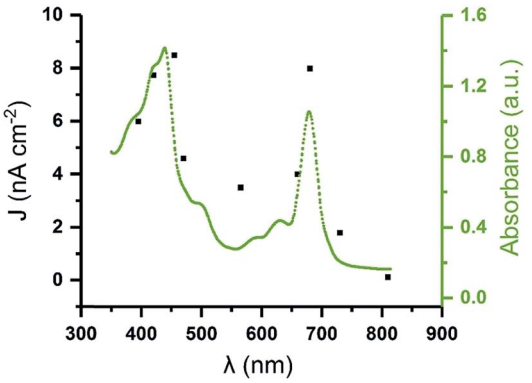

Fig. 4 Action spectra (black square) representing the photocurrent density (left *Y* axis) *vs.* irradiation wavelength of the PSI-SLB/SAM/Au. The room temperature absorption spectra of PSI (green line, right *Y* axis) matches the photocurrent response of PSI-SLB on substrates.

electrodes, respectively. All photocurrents are reported for the fourth light on/off pulse in Fig. 5a as the photocurrent density reaches a steady value at the fourth pulse (Fig. 5b). The aforementioned data are obtained for PSI-proteoliposome reconstituted with $C_{\mathrm{Trit}} = 12.0$ mM. The SAM treated Au substrate without the addition of PSI generated a photocurrent of ~1 nA cm^{-2} (the ochre line is moved up for ease of visualization, Fig. 5a). The comparison of the maximum photocurrent densities obtained from the electrochemical CA measurements on various SAM substrates with different terminal chemistries and PSI-proteoliposomes reconstituted with different detergent concentrations ($C_{\mathrm{Trit}} = 4.0$, 8.0 and 12.0 mM) reveals almost similar photocurrents to the one obtained from the PSI/C_4COOH SAM/Au substrate with a minor increase observed in the case of PSI-SLB/SAM/Au samples for PSI-proteoliposomes reconstituted with $C_{\mathrm{Trit}} = 12$ mM (ESI, Fig. S1†). This observation contradicted our initial hypothesis that PSI confinements in a biomimetic membrane framework will promote photocurrent enhancements.

In an effort to explain these observations, the surface topography images of PSI-SLB treated C_4–COOH SAM/Au, C_4–OH SAM/Au and C_6–OH SAM/Au substrates acquired from AFM measurements are presented in Fig. 6a–d. These images reveal a semi-sparse monolayer of PSIs within the SLB, as well as the presence of some intact liposomes which have not fully collapsed on the SAM layers (arrow indicators in Fig. 6b–d). However, in the case of the deposition of individual PSI trimers onto the alkanethiolate SAM/Au substrates, as shown in Fig. 6a, a relatively uniform PSI monolayer formation with high surface coverage, as reported in our earlier studies, is observed.[21,33] It should be noted that although only PSI deposition on the C_4COOH SAM/Au substrate is shown in Fig. 6a, PSI depositions on C_4OH SAM/Au and C_6OH SAM/Au substrates also indicated similar dense monolayer coverage.

The aforementioned differences in the surface coverage (number of immobilized PSIs per unit area of the electrode) can provide a plausible explanation for the relatively low photocurrent enhancement achieved in the case of membrane-bound PSI/SAM/Au electrode cases. In order to further investigate our rationale, the number of PSI complexes assembled per unit surface area was subsequently counted from the respective AFM images. Specifically, the PSI complexes were identified based on the typical average protein diameters of ~22 nm as well as average heights of ~9 nm which are commensurate with the expected dimensions of the cyanobacterial PSI trimeric complexes (see Fig. 2).[21,33] Upon normalization of the measured photocurrent densities with respect to the number of PSI complexes immobilized on the respective substrates (as calculated from imaging analysis of AFM topographies), the photocurrent enhancements for the reconstituted PSI-proteoliposomes as compared to those from

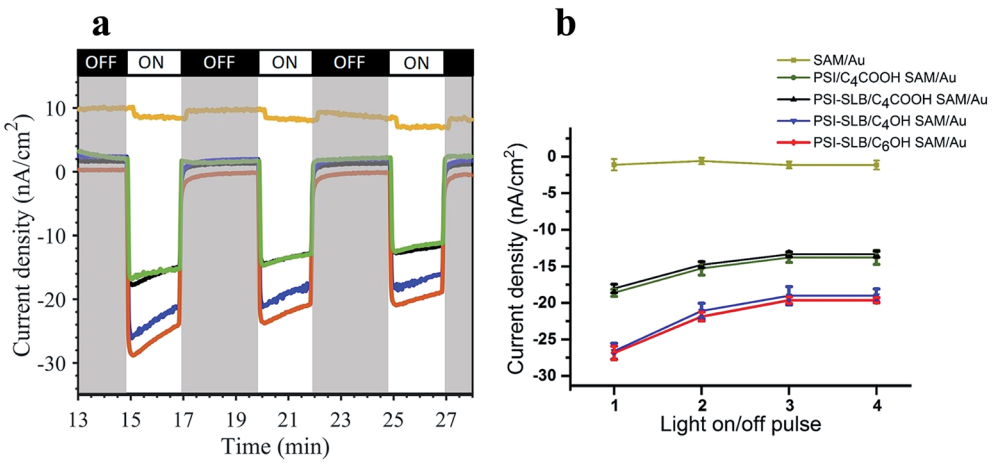

Fig. 5 (a) Chronoamperometry data indicating a maximum 14.5 ± 0.9 nA cm^{-2} cathodic photocurrent from the PSI/C_4COOH SAM/Au substrate at OCV *vs.* Ag/AgCl under illumination ($\lambda = 660$ nm) under aerobic conditions (green line) along with subsequent photocurrent enhancements for PSI-SLB assembled on C_4COOH–thiol/Au (black line), C_4OH–thiol/Au (blue line) and C_6OH–thiol/Au (red line). Photocurrents from the SAM/Au substrate without any PSI (ochre line) are moved up for ease of visualization; (b) average photocurrent densities for SAM/Au, PSI/SAM/Au and PSI-SLB/SAM/Au substrates from the respective chronoamperometry data in (a) plotted as a function of the number of light on/off pulses to indicate the emergence of steady photocurrent densities after the fourth pulse.

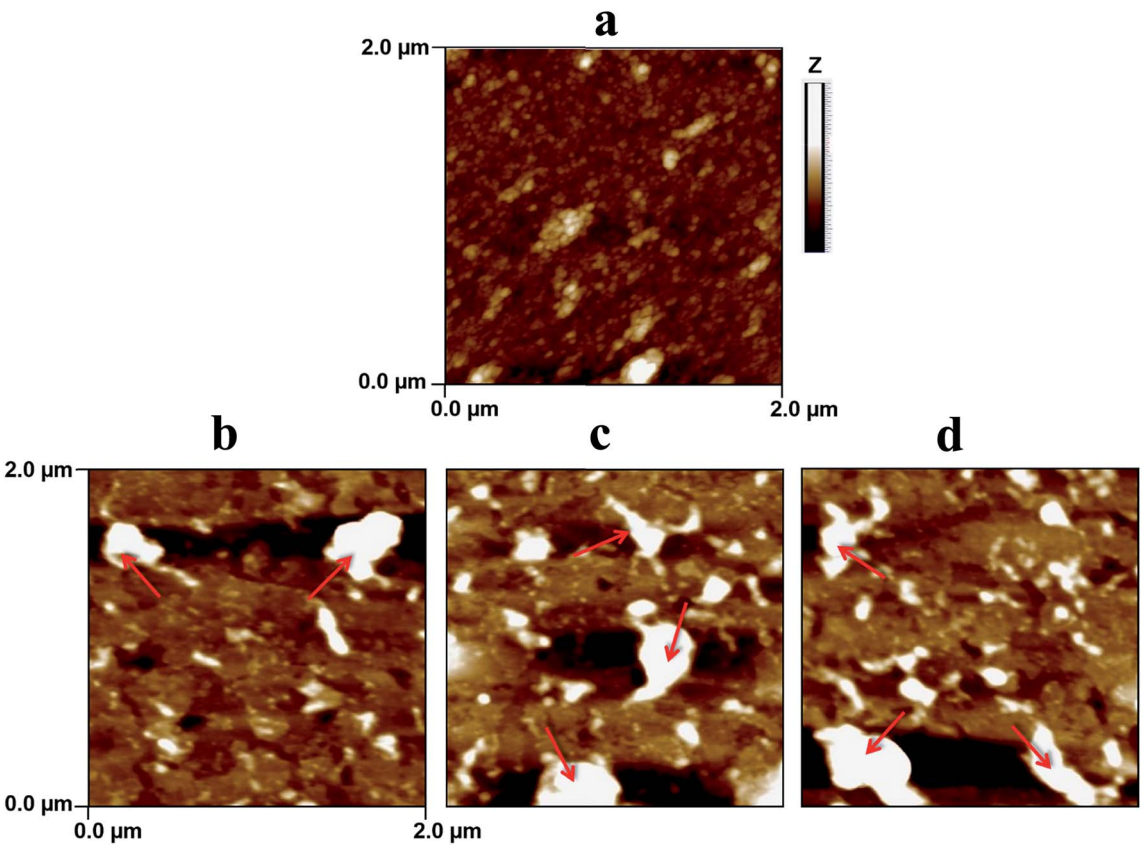

Fig. 6 AFM images showing the surface topographies of: (a) PSI/C_4COOH SAM/Au; (b) PSI-SLB/C_4COOH SAM/Au; (c) PSI-SLB/C_4OH SAM/Au and (d) PSI-SLB/C_6OH SAM/Au. Red arrows indicate the presence of liposomes not fully collapsed onto the SAM substrates.

individual PSI trimers immobilized on SAM/Au substrates immediately become evident (see Fig. 7). Specifically, the representative case of PSI-proteoliposomes reconstituted with $C_{Trit} = 12$ mM (*i.e.*, the optimal reconstitution case based on our earlier studies)[33] indicates ~3–4 times enhancement in the photocurrent obtained from the PSI-SLB/C_4OH SAM/Au substrate when compared to that from the PSI/C_4COOH SAM/Au substrate. Also, based on the AFM images and photocurrent measurements, our observations indicate the possibility of a better assembly and hence higher performance for PSI-SLBs formed on OH-terminated SAMs.

Achieving significantly high electron transfer rates per PSI complex (hundreds of μA mg^{-1} PSI)[30,37] requires direct electron transfer between the electrode and PSI, high packing density, and systematic confinements promoting the correct orientation of PSIs on the substrate. We have successfully achieved a dense and uniform monolayer of PSI on the SAM-treated substrates, however the relatively low photocurrent of 1.813 μA mg^{-1} PSI (considering 14.5 nA cm^{-2}, 0.008 mg PSI per cm^2) obtained from these substrates might be due to the lack of direct electron transfer between the electrode and PSI, tailored orientation and confinements. Semi-sparse monolayers of PSIs within the SLB, in the presence of some intact liposomes showed enhanced photocurrents of 5.06 μA mg^{-1} PSI (13.5 nA cm^{-2}, 0.0027 mg PSI per cm^2), 7.88 μA mg^{-1} PSI (18 nA cm^{-2}, 0.0023 mg PSI per cm^2) and 7.5 μA mg^{-1} PSI (20 nA cm^{-2}, 0.0027 mg PSI per cm^2) for PSI/C_4COOH SAM/Au, PSI/C_4OH SAM/Au and PSI/C_6OH SAM/Au substrates, respectively. The relatively low electron transfer rates per PSI complex for these cases may suggest that the direct electron transfer between the electrode and PSI is the limiting factor in the photocurrent generation.

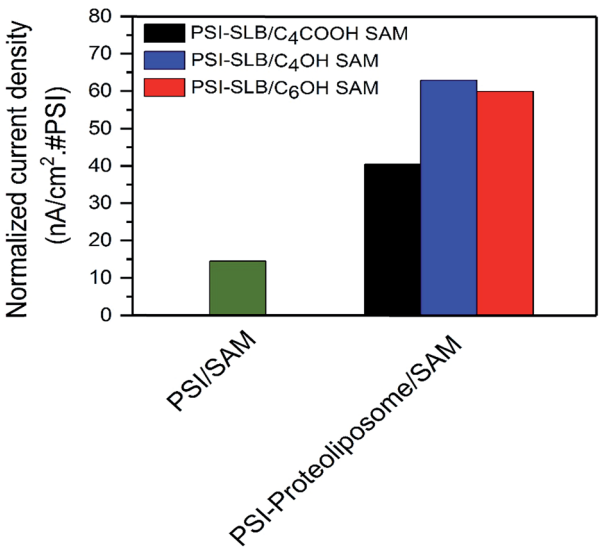

Fig. 7 Comparisons for the maximum photocurrent densities normalized with respect to the number of PSI complexes assembled on the respective substrates. Representative results compared here for PSI-SLB/SAM/Au substrates made from PSI-proteoliposomes reconstituted with 12 mM TX-100.

It needs to be pointed out here that recent studies on photosystem II integrated into electrodes had revealed that in the absence of the membrane environment, short circuiting of electron transfer between electrode materials and surface exposed chlorophylls occurs in photosystems which results in the underperformance of these systems.[38,39] It was additionally proposed that this short circuiting might promote rapid deactivation of the photosynthetic proteins.[39] To this end, PSII integrated in devices showed very fast deactivation[40] with a half-life of ~4 min for PSII wired to electrodes *via* redox-active polymers. Even PSI, that is well known as a highly robust membrane protein, indicated a half-life of ~15 min when integrated into electron conducting matrices (redox hydrogel film) in the absence of any lipid membranes.[37] On the contrary, measurements from the membrane-bound PSIs in our system indicate stable photocurrents even after 30 min. Such observations further indicate that synthetic lipid membranes, when used as well-defined protein–pigment scaffolds, can minimize unwanted charge transfer processes and enhance the stability of the pigment-containing systems.

Force spectroscopy of the PSI-SLB system

Herein, we resort to high resolution AFM measurements in aqueous solution to obtain more direct evidence of the successful formation of PSI-proteoliposomes in our SLB assemblies. Specifically, atomic force spectroscopy on the PSI-SLB assemblies on atomistically flat gold surfaces is carried out. AFM topography images of flat gold before and after exposure to the lipid vesicles comprising pure DPhPG were first recorded (see ESI, Fig. S2a, b† respectively). After vesicle exposure, the surface shown in Fig. S2b† exhibited uniform bilayer formation. Subsequently, force spectroscopy characterizations were performed on flat gold and the representative force–distance curves were recorded (as shown in the ESI, Fig. S3†). Force–distance curves obtained on bare gold substrates showed no breakthrough. Multiple force–distance curves were obtained on bare gold that were used to calibrate the system to generate the inverse optical lever sensitivity of our forced spectroscopy system as 61.714 nm nA^{-1}. Subsequently, force–distance curves acquired on a DPhPG bilayer exhibited a single breakthrough. The extend–retract displacement *versus* deflection curves were used to estimate the thickness of the bilayer as described by Choi and Dimitriadis.[41] A measured thickness of 5.2 ± 0.4 nm (for n = 60 curves) corroborated the expected values for the control lipid bilayer systems.

Finally, we perform AFM force spectroscopy on PSI-SLB assemblies on identical flat gold surfaces (Fig. 8). Data from force–distance curves acquired from different regions of PSI-SLBs provide an average breakthrough distance for a single breakthrough to be 5.2 ± 0.4 nm (n = 90 curves) on a plain lipid bilayer area (point I) and 7.8 ± 0.9 nm (n = 110 curves) on a PSI encapsulated SLB area (point II). We note that the expected PSI-SLB thickness is approximately 9.0 nm.[42] The fluid nature of the membrane and the statistical nature of the breakthrough affect the standard deviation of the breakthrough thickness.[41,43] Hence, the smaller measured thickness might be due to the compression of PSI as a result of AFM induced elastic deformation prior to the breakthrough. From the measurement points I and II, the yield threshold forces at which breakthroughs occur in the force–distance curves are calculated to be ~1.95 nN (n = 90 curves) and ~2.28 nN (n = 110 curves), respectively. One needs to bear in mind that double breakthroughs were typically observed on force–distance curves

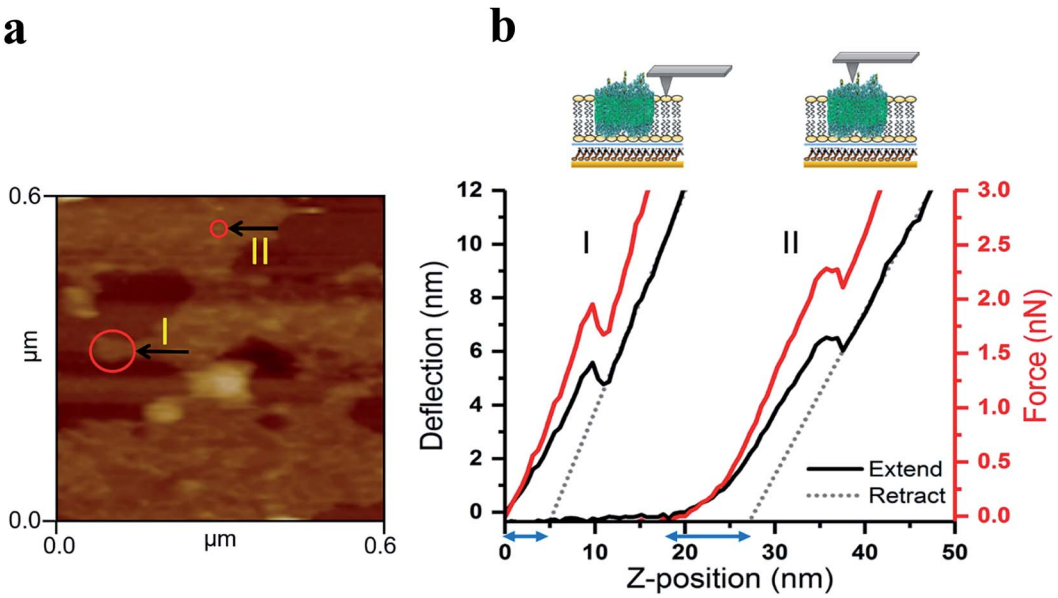

Fig. 8 Force spectroscopy measurements on pure SLB and PSI-SLB regions marked as I and II respectively in (a) generate the extend–retract curves of the DPhPG bilayer and PSI-SLB respectively as shown in (b); extend–retract displacement *vs.* deflection curves (black line, left *Y* axis) in (b) indicate the thickness of layers along the *Z*-position (nm) (blue arrows on the *X*-axis). The yield threshold force at which breakthrough occurs is given in force–distance curves (red line, right *Y* axis).

obtained on PSI-SLBs that are consistent with multilayer formations. Such double breakthroughs might indicate the presence of PSIs physisorbed on a DPhPG bilayer or multilayers of DPhPG.

Conclusions

The work presented here demonstrates the systematic photocurrent enhancements from PSI, the transmembrane photosynthetic protein, assembled onto electrode interfaces *via* protein confinements in synthetic supported lipid bilayer (SLB) scaffoldings. Specifically, the SLBs were fabricated from PG-based negatively charged liposomes (DPhPG) that mimic the natural thylakoid membrane housing of PSI. This study paves the way for the successful fabrication of efficient biotic–abiotic interfaces for PSI-based bio-hybrid photoelectrochemical energy conversion devices in future. AFM imaging and force spectroscopy of PSI-SLB on flat gold provide direct evidence of the successful encapsulation of PSI in the proteoliposomes. Finally, detailed electrochemical measurements on PSI-SLBs supported on various alkanethiolate SAM/Au surfaces indicate up to 4–5 times enhancements in photocurrent densities when compared to the measurements from a dense monolayer of individual PSI on SAM/Au substrates. The results presented here motivate us to raise the fundamental questions regarding the relative roles of quantum coherence effects, conformational changes in the chlorophyll networks and/or simply, improved PSI orientations under membrane confinements in tuning the photocurrent enhancements from PSI as a result of microenvironment alterations due to PSI confinements in lipid bilayers. Although such questions are of tremendous interest to the biophysics community involved in quantum biology research, conclusive evidence of it is still elusive and requires rigorous ultra-fast time-resolved measurements that are part of our current ongoing research. From an application standpoint, the current study underscores the significance of a fundamental understanding of the unique optoelectronic properties of PSI under biomimetic confinement in advancing the design of photochemical energy conversion and artificial photosynthetic systems.

Conflicts of interest

There are no conflicts to declare.

Acknowledgements

The authors would like to acknowledge the University of Tennessee Advanced Microscopy and Imaging Center and Bioanalytical Resources Facility for instrument use, and Dr John Dunlap and Dr Edward Wright for scientific and technical assistance. We thank Dr Graham J. Taylor for helping us preparing the liposome suspension. Also we thank Dr Mahdi Hejazi and Dr Athina Zouni (Humboldt-University of Berlin, Institute of Biology, Biophysics of Photosynthesis, Berlin, Germany) for providing the photosystem I. This work was funded in part by the Sustainable Energy Education and Research Center (SEERC) at University of Tennessee, Knoxville and the Gibson Family Foundation.

References

1 A. Badura, T. Kothe, W. Schuhmann and M. Rogner, *Energy Environ. Sci.*, 2011, **4**, 3263–3274.
2 N. Terasaki, N. Yamamoto, T. Hiraga, I. Sato, Y. Inoue and S. Yamada, *Thin Solid Films*, 2006, **499**, 153–156.
3 D. Gerster, J. Reichert, H. Bi, J. V. Barth, S. M. Kaniber, A. W. Holleitner, I. Visoly-Fisher, S. Sergani and I. Carmeli, *Nat. Nano*, 2012, **7**, 673–676.
4 P. N. Ciesielski, A. M. Scott, C. J. Faulkner, B. J. Berron, D. E. Cliffel and G. K. Jennings, *ACS Nano*, 2008, **2**, 2465–2472.
5 G. LeBlanc, G. Chen, G. K. Jennings and D. E. Cliffel, *Langmuir*, 2012, **28**, 7952–7956.
6 D. Gunther, G. LeBlanc, D. Prasai, J. R. Zhang, D. E. Cliffel, K. I. Bolotin and G. K. Jennings, *Langmuir*, 2013, **29**, 4177–4180.
7 G. LeBlanc, K. M. Winter, W. B. Crosby, G. K. Jennings and D. E. Cliffel, *Adv. Energy Mater.*, 2014, **4**, 5.
8 L. Frolov, Y. Rosenwaks, S. Richter, C. Carmeli and I. Carmeli, *J. Phys. Chem. C*, 2008, **112**, 13426–13430.
9 I. Carmeli, M. Mangold, L. Frolov, B. Zebli, C. Carmeli, S. Richter and A. W. Holleitner, *Adv. Mater.*, 2007, **19**, 3901–3905.
10 S. M. Kaniber, M. Brandstetter, F. C. Simmel, I. Carmeli and A. W. Holleitner, *J. Am. Chem. Soc.*, 2010, **132**, 2872–2873.
11 N. Terasaki, N. Yamamoto, M. Hattori, N. Tanigaki, T. Hiraga, K. Ito, M. Konno, M. Iwai, Y. Inoue, S. Uno and K. Nakazato, *Langmuir*, 2009, **25**, 11969–11974.
12 N. Terasaki, N. Yamamoto, T. Hiraga, Y. Yamanoi, T. Yonezawa, H. Nishihara, T. Ohmori, M. Sakai, M. Fujii, A. Tohri, M. Iwai, Y. Inoue, S. Yoneyama, M. Minakata and I. Enami, *Angew. Chem., Int. Ed.*, 2009, **48**, 1585–1587.
13 N. Terasaki, N. Yamamoto, K. Tamada, M. Hattori, T. Hiraga, A. Tohri, I. Sato, M. Iwai, M. Iwai, S. Taguchi, I. Enami, Y. Inoue, Y. Yamanoi, T. Yonezawa, K. Mizuno, M. Murata, H. Nishihara, S. Yoneyama, M. Minakata, T. Ohmori, M. Sakai and M. Fujii, *Biochim. Biophys. Acta, Bioenerg.*, 2007, **1767**, 653–659.
14 L. Frolov, Y. Rosenwaks, C. Carmeli and I. Carmeli, *Adv. Mater.*, 2005, **17**, 2434–2437.
15 R. K. Le, M. Raeeszadeh-Sarmazdeh, E. T. Boder and P. D. Frymier, *Langmuir*, 2015, **31**, 1180–1188.
16 B. S. Ko, B. Babcock, G. K. Jennings, S. G. Tilden, R. R. Peterson, D. Cliffel and E. Greenbaum, *Langmuir*, 2004, **20**, 4033–4038.
17 M. Ciobanu, H. A. Kincaid, V. Lo, A. D. Dukes, G. K. Jennings and D. E. Cliffel, *J. Electroanal. Chem.*, 2007, **599**, 72–78.
18 M. Ciobanu, H. A. Kincaid, G. K. Jennings and D. E. Cliffel, *Langmuir*, 2005, **21**, 692–698.
19 C. J. Faulkner, S. Lees, P. N. Ciesielski, D. E. Cliffel and G. K. Jennings, *Langmuir*, 2008, **24**, 8409–8412.
20 A. K. Manocchi, D. R. Baker, S. S. Pendley, K. Nguyen, M. M. Hurley, B. D. Bruce, J. J. Sumner and C. A. Lundgren, *Langmuir*, 2013, **29**, 2412–2419.

21 D. Mukherjee, M. May and B. Khomami, *J. Colloid Interface Sci.*, 2011, **358**, 477–484.
22 D. Mukherjee, M. Vaughn, B. Khomami and B. D. Bruce, *Colloids Surf., B*, 2011, **88**, 181–190.
23 T. Bennett, H. Niroomand, R. Pamu, I. Ivanov, D. Mukherjee and B. Khomami, *Phys. Chem. Chem. Phys.*, 2016, **18**, 8512–8521.
24 K. Brettel and W. Leibl, *Biochim. Biophys. Acta, Bioenerg.*, 2001, **1507**, 100–114.
25 G. F. White, K. I. Racher, A. Lipski, F. R. Hallett and J. M. Wood, *Biochim. Biophys. Acta, Bioenerg.*, 2000, **1468**, 175–186.
26 N. Das, D. T. Murray and T. A. Cross, *Nat. Protoc.*, 2013, **8**, 2256–2270.
27 H.-X. Zhou and T. A. Cross, *Annu. Rev. Biophys.*, 2013, **42**, 361–392.
28 P. O. Saboe, C. E. Lubner, N. S. McCool, N. M. Vargas-Barbosa, H. Yan, S. Chan, B. Ferlez, G. C. Bazan, J. H. Golbeck and M. Kumar, *Adv. Mater.*, 2014, **26**, 7064–7069.
29 N. D. Kirchhofer, M. A. Rasmussen, F. W. Dahlquist, S. D. Minteer and G. C. Bazan, *Energy Environ. Sci.*, 2015, **8**, 2698–2706.
30 P. O. Saboe, E. Conte, S. Chan, H. Feroz, B. Ferlez, M. Farell, M. F. Poyton, I. T. Sines, H. Yan, G. C. Bazan, J. Golbeck and M. Kumar, *J. Mater. Chem. A*, 2016, **4**, 15457–15463.
31 K. R. Stieger, D. Ciornii, A. Kolsch, M. Hejazi, H. Lokstein, S. C. Feifel, A. Zouni and F. Lisdat, *Nanoscale*, 2016, **8**, 10695–10705.
32 K. R. Stieger, S. C. Feifel, H. Lokstein, M. Hejazi, A. Zouni and F. Lisdat, *J. Mater. Chem. A*, 2016, **4**, 17009–17017.
33 H. Niroomand, D. Mukherjee and B. Khomami, *Sci. Rep.*, 2017, **7**, 2492.
34 J. Kern, B. Loll, C. Lüneberg, D. DiFiore, J. Biesiadka, K. D. Irrgang and A. Zouni, *Biochim. Biophys. Acta, Bioenerg.*, 2005, **1706**, 147–157.
35 D. Lichtenberg and Y. Barenholz, in *Methods Biochem. Anal.*, John Wiley & Sons, Inc., 2006, ch. 7, pp. 337–462, DOI: 10.1002/9780470110546.
36 H. Niroomand, G. A. Venkatesan, S. A. Sarles, D. Mukherjee and B. Khomami, *J. Membr. Biol.*, 2016, **249**, 523–538.
37 T. Kothe, S. Pöller, F. Zhao, P. Fortgang, M. Rögner, W. Schuhmann and N. Plumeré, *Chem.–Eur. J.*, 2014, **20**, 11029–11034.
38 M. M. Nowaczyk and N. Plumere, *Nat. Chem. Biol.*, 2016, **12**, 990–991.
39 J. Z. Zhang, K. P. Sokol, N. Paul, E. Romero, R. van Grondelle and E. Reisner, *Nat. Chem. Biol.*, 2016, **12**, 1046–1052.
40 K. P. Sokol, D. Mersch, V. Hartmann, J. Z. Zhang, M. M. Nowaczyk, M. Rogner, A. Ruff, W. Schuhmann, N. Plumere and E. Reisner, *Energy Environ. Sci.*, 2016, **9**, 3698–3709.
41 E. J. Choi and E. K. Dimitriadis, *Biophys. J.*, 2004, **87**, 3234–3241.
42 P. Fromme, P. Jordan and N. Krauß, *Biochim. Biophys. Acta, Bioenerg.*, 2001, **1507**, 5–31.
43 V. Franz, S. Loi, H. Müller, E. Bamberg and H.-J. Butt, *Colloids Surf., B*, 2002, **23**, 191–200.